



# Dynamic modification of pore opening of SAPO-34 by adsorbed surface methoxy species during induction of catalytic methanol-to-olefins reactions

B.T.W. Lo<sup>a,1</sup>, L. Ye<sup>a,1</sup>, G.G.Z. Chang<sup>a</sup>, K. Purchase<sup>a</sup>, S. Day<sup>b</sup>, C.C. Tang<sup>b</sup>, D. Mei<sup>c,\*</sup>, S.C.E. Tsang<sup>a,\*</sup>

<sup>a</sup> Department of Chemistry, University of Oxford, Oxford, OX1 3QR, UK

<sup>b</sup> Diamond Light Source Ltd, Harwell Science and Innovation Campus, Didcot, Oxfordshire, OX11 0DE, UK

<sup>c</sup> Pacific Northwest National Laboratory, Physical and Computational Sciences Directorate & Institute for Integrated Catalysis, Richland, WAPO, Box 999, USA

## ARTICLE INFO

### Keywords:

Methanol conversion  
SAPO-34 zeolite  
Synchrotron x-ray powder diffraction  
Product distribution  
Surface methoxy Surface

## ABSTRACT

Here, we report that the 8-membered ring pore opening of SAPO-34 zeolite can be significantly modified by an adsorbed surface methoxy species (SMS) during the induction period of the catalytic methanol-to-olefins process, which offers molecular sieving properties. It is due to the physical obstruction caused by the surface methoxy species, which also modifies the adsorption properties of other hydrocarbons. Synchrotron X-ray powder diffraction and Rietveld refinement reveal that the SMS is dynamically created from methanol dehydration on a Brønsted acid site near the narrow pore windows. Thus, industrially desirable lower olefins such as ethylene and propylene can be favourably made at the expense of higher olefins. The crystal structures and fundamental understanding in altering the olefin selectivity during induction may allow rational optimisation in catalytic performance under complex fluidised conditions. This work offers additional but alternative insights to the 'dual cycle' mechanistic study of the catalytic methanol-to-olefins process.

## 1. Introduction

In the formulation of the strategic national energy policies of many countries, the uneven geographical distribution of fossil fuels and associated CO<sub>2</sub> emissions are significant issues. As a result, identifying alternative fuels and platform chemicals are critical. Typically, methanol from coal or biomass processing from oil-starved countries is regarded as a potential alternative to mitigate these problems [1]. It can be used as a direct fuel or key chemical for the synthesis of commodity chemicals through various methanol-to-hydrocarbons (MTH) processes, such as to olefins (MTO), aromatics (MTA) and gasoline (MTG), etc. [2,3]. It is anticipated that the reliance over methanol will continue in the foreseeable future, due to the rapidly growing demand for consumer goods. Most of the industrial MTH processes employ the use of zeolite catalysts. It is however not yet clear how the specific hydrocarbon products are produced from the methanol feed and the influence of zeolite structure on their pathways. It is generally accepted that, particularly by the extensive work by Kolboe and co-workers, the MTO reaction mechanism involves a dual cycle mechanism which involves both aromatic and alkene cycles [4–9]. Methanol molecules first adsorb onto an interior Brønsted acid sites (BAS) in zeolites, then they rapidly dehydrate and form C–C bonds and polymerise at high temperature

forming a 'hydrocarbon pool' (HCP) intermediate in the induction period. Methyl (CH<sub>3</sub>) species from methanol decomposition or dehydration are believed to be constantly fed into the HCP while alkenes are split off. Attempts have been carried out to analyse the transient products to form or decompose from the HCP at different time-on-stream (TOS) in hope to get clues on the mechanisms [10]. However, this proves to be difficult due to some intrinsically fast reactions complicated by secondary reactions with aromatics and carbonaceous depositions that can also modify zeolite catalysis in a dynamic manner. Nevertheless, it has been independently demonstrated that the HCP contains polymethylbenzene as the primary intermediate at steady state, where the degree of methylation depends on the topology the zeolite porous structure and spatial arrangement of the BAS [11].

Previous reports on the pore size effect of zeolites on product selectivity have been summarised by Olsbye et al. [12]. The choice of zeolite catalysts depends on the product selectivity, e.g. SAPO-34 primarily gives lower olefins, but H-ZSM-5 mostly gives aromatics [13]. The framework structures of zeolites with respect to the substrates and products have been studied extensively by various characterisation techniques, including X-ray diffraction [14], BET/BJH methods [15] and isotopic switch experiments [16], etc. The product size/shape selectivity is commonly attributed to the mass transfer and transition

\* Corresponding authors.

E-mail addresses: [donghai.mei@pnnl.gov](mailto:donghai.mei@pnnl.gov) (D. Mei), [edman.tsang@chem.ox.ac.uk](mailto:edman.tsang@chem.ox.ac.uk) (S.C.E. Tsang).

<sup>1</sup> These authors contributed equally.

state effects [17]. The former circumvents merely the formation or diffusion of ‘over-sized’ products by its zeolite framework, by acting as a molecular sieve. Whereas, the latter is caused by the confined space within the zeolite framework, which influences the formation of certain transition state species. However, such assumption is based on the rigid models of zeolite frameworks or carbonaceous species filled zeolites with respect to product molecules, where the dynamic modifications or interactions of the pore openings in proximity to the active BAS by reaction species are commonly ignored.

The industrial MTO process requires the capture of product gases of an appropriate composition under a fixed contact time before the air-regeneration of the carbonaceous-fouled zeolite catalyst in a fluidised-bed reactor. Typically, a minimum induction period of about 20 min, dependent on the reaction conditions, is applied to the industrial MTO process over the SAPO-34 catalyst [6]. During the induction, the product gas is empirically shown to contain large quantity of *i*-butene, pentene and other C<sub>5</sub><sup>+</sup>. However, at steady state, more desirable lower olefins, such as ethylene and propylene, are the major products, which match the downstream needs for the synthesis of polyethylene (PE) and polypropylene (PP) [18]. Thus, a rational reduction of undesirable induction phase for higher olefins and the end of the phase for carbonaceous deposition would be of both academic and practical importance.

By using synchrotron X-ray powder diffraction (SXRD) and Rietveld refinement, our group have recently revealed the structures of organic adsorbates (such as pyridine, ammonia and methanol) even at low surface coverage inside various zeolite frameworks [19–23]. Based on diffraction evidence, the bond distances and angles of these organic species about the surface BAS can be measured within experimental errors, which could offer addition information to the traditional spectroscopic techniques. In light of these works, we have designed a low-dead-volume capillary reactor gas-cell to study the catalytic activity-structure relationship, using the optimised high-brightness synchrotron X-ray beam at Beamline I11 in Diamond, UK. Hereby, we report a dynamic modification of the molecular 8-membered ring (MR) opening to the super-cage of the pore opening in SAPO-34 during the early stage of MTO induction process. It is found that a low degree of carbonaceous deposition in confined space does not offer much blockage to the gaseous products. Using SXRD-mass spectroscopy (MS) with Rietveld refinement, selective gas uptake and density functional theory (DFT) calculations, it is demonstrated for the first time that the molecular entry window of the 8-MR pore opening of SAPO-34 is modified dynamically by a surface methoxy species (SMS) at a steady state on the zeolite framework. This offers a molecular sieving effect and modifies the adsorption properties of the zeolite. Both facilitate the desirable C<sub>2</sub><sup>=</sup>/C<sub>3</sub><sup>=</sup> production, and deny higher olefins from passage after the induction period. Simply, the SMS renders a ‘door-keeping’ effect to deny the less desirable n-C<sub>4</sub><sup>=</sup> products.

## 2. Experimental

### 2.1. Synchrotron x-ray powder diffraction (SXRD) and Rietveld refinements

SXRD data were collected at Beamline I11, Diamond Light Source, Harwell, UK [24]. The energy of the incident X-ray flux was set at 15 KeV. The wavelength and 2θ-zero point were refined using a diffraction pattern obtained from a high-quality silicon powder (SRM640c). High-resolution SXRD data were obtained from the zeolite samples using the multi-analyser crystals (MAC) detectors. The patterns were collected in the 2θ range 0–150° with 0.003° data binning. Each MAC pattern was collected for an hour for good statistics. A capillary reactor cell was specifically designed for this reaction in the SAPO-34 sample under SXRD in a controllable manner, see Fig. S1 in the Supplementary Materials (SM) (see SM/methods for more information).

For the Rietveld refinement analyses, similar procedures as our

**Table 1**

Product distribution of SAPO-34 of the MTO process at industrial reaction conditions at 460 °C with 100% conversion of methanol (data provided by SRIPT-SINOPEC). The powder catalyst was pressed into a pallet and loaded in a fixed-bed reactor.

TOS (min)	Product distribution (wt%)									
	CH <sub>4</sub>	C <sub>2</sub> H <sub>4</sub>	C <sub>2</sub> H <sub>6</sub>	C <sub>3</sub> H <sub>6</sub>	C <sub>3</sub> H <sub>8</sub>	(CH <sub>3</sub> ) <sub>2</sub> O	MeOH	C <sub>4</sub> <sup>=</sup>	C <sub>5</sub> <sup>+</sup>	C <sub>2</sub> <sup>=</sup> + C <sub>3</sub> <sup>=</sup>
5	1.7	29.0	0.9	35.2	8.2	0.1	0.0	18.0	6.9	64.1
10	1.9	31.1	1.1	35.8	6.7	0.0	0.0	17.2	6.1	66.9
20	2.5	37.4	1.1	35.4	3.6	0.0	0.0	14.8	5.2	72.8
30	2.4	42.6	1.0	35.2	2.1	0.0	0.0	12.4	4.3	77.8
35	2.5	44.5	0.9	34.7	1.6	0.0	0.0	11.5	4.2	79.2
40	2.4	46.1	0.8	34.6	1.3	0.1	0.0	10.6	4.0	80.7
45	2.5	47.5	0.8	34.2	1.0	0.1	0.0	9.9	3.9	81.7
50	2.5	48.6	0.7	33.9	0.9	0.2	0.0	9.3	3.8	82.5
55	2.6	48.9	0.7	33.3	0.7	0.7	0.0	8.8	4.3	82.2
60	2.6	49.3	0.6	32.6	0.6	2.2	0.0	8.3	3.7	81.9

previous works have been carried out (the details can also be found in SM) [19–23].

## 3. Results

The commercial powder SAPO-34 sample (space group of R-3) has a surface area of 510 m<sup>2</sup> g<sup>−1</sup>. It has an average cubic particle size of 5 μm that is ideal for Rietveld refinement. From the structural formula of Al<sub>0.81</sub>Si<sub>0.19</sub>PO<sub>2</sub> (silicon-doped aluminium phosphate), it contains 3.4 BAS per unit cell and a total BAS concentration of 1.1 mmol g<sup>−1</sup>. We first studied the MTO induction process over SAPO-34 under the typical industrial conditions, using a fixed-bed packed reactor at 460 °C at SRIPT-SINOPEC where 100% conversion of methanol was achieved. Table 1 displays the product distribution. Despite the total conversion of methanol at the early stage of induction, the C<sub>2</sub><sup>=</sup> + C<sub>3</sub><sup>=</sup> selectivity increases progressively over longer TOS, from 64.1% to 82.5% after 50 min TOS. Interestingly, the corresponding C<sub>4</sub><sup>=</sup> selectivity decreases over longer TOS from 18.0% to 9.3%. The propane (C<sub>3</sub>H<sub>8</sub>) concentration also decreases over longer TOS, which is in favour of the desired olefinic products, as previously discussed. This is extremely useful from the industrial perspective if we can finely tune the productivity towards the desired olefin products with shorter TOS. However, the reasons behind the change in product selectivity in the time course have not yet been well-studied in the literature.

## 4. Discussion

To rationalise time-dependent product selectivities in catalysis, we recently designed a high-pressure, low-dead-volume catalytic capillary gas-cell for SXRD measurements in Beamline I11, Diamond Light Source, UK (see SM/Methods and Figure S1). A powder SAPO-34 sample was first kept in the gas-cell (diameter of 0.7 mm) under a He flow rate of 2.5 mL min<sup>−1</sup> at 1 atmosphere via a methanol saturator (kept at RT). While analysing the out-let gas using a mass spectrometer (MS), the SAPO-34 sample was scanned with parallel but high-brightness synchrotron X-ray beam at an energy of 15 keV, to study the structure-activity relationship. The sample was first heated to 460 °C and injected with a stream of methanol vapour under a He flow rate of 2.5 mL min<sup>−1</sup> via a methanol saturator (kept at RT at 1 atmosphere) for 2-min TOS. After 2 min of methanol injection, the sample was kept 5 min to remove any adsorbed methanol at 460 °C. Then the sample was brought down to RT, where SXRD was collected. This is followed by repeated 2-min TOS of methanol injection at 460 °C, 5 min of residue removal at 460 °C, and SXRD scanning at RT. The on-line MS of methanol substrate and C<sub>2</sub><sup>=</sup>-C<sub>4</sub><sup>=</sup> were simultaneously monitored (traces

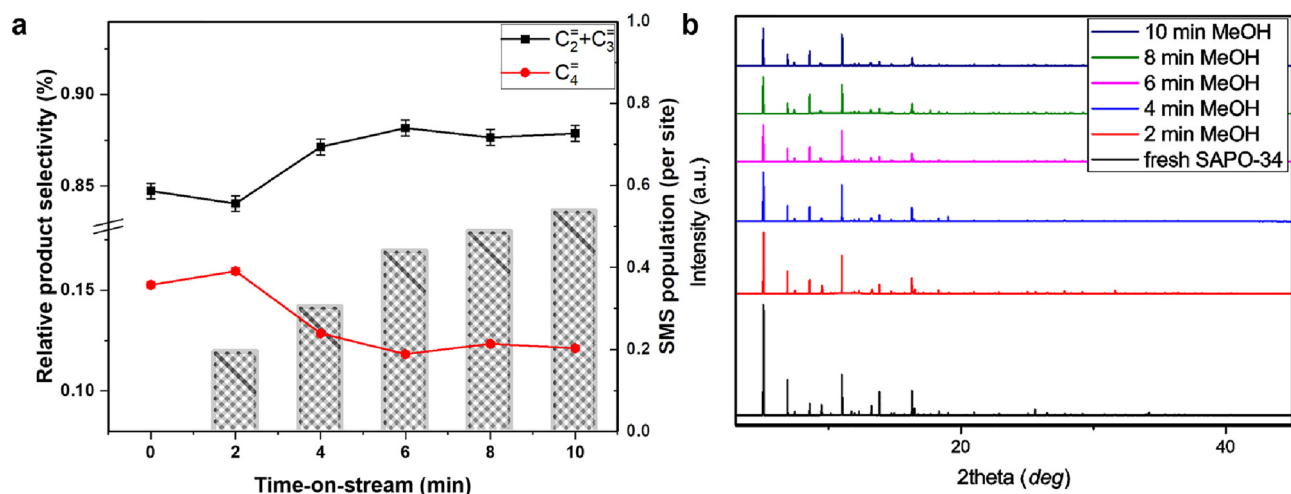


**Fig. 1.** (a) Analysis of the relative  $C_2^= + C_3^=$  (black line) and  $C_4^=$  (red line) selectivities from the on-line mass spectra, with the population of the SMS ( $CH_3-O_2$ ) derived from the SXR measurements (bar chart), and (b) high-resolution SXR profiles measured at room temperature, after injection of methanol vapour over SAPO-34 (TOS as labelled). (For interpretation of the references to colour in this figure legend, the reader is referred to the web version of this article.).

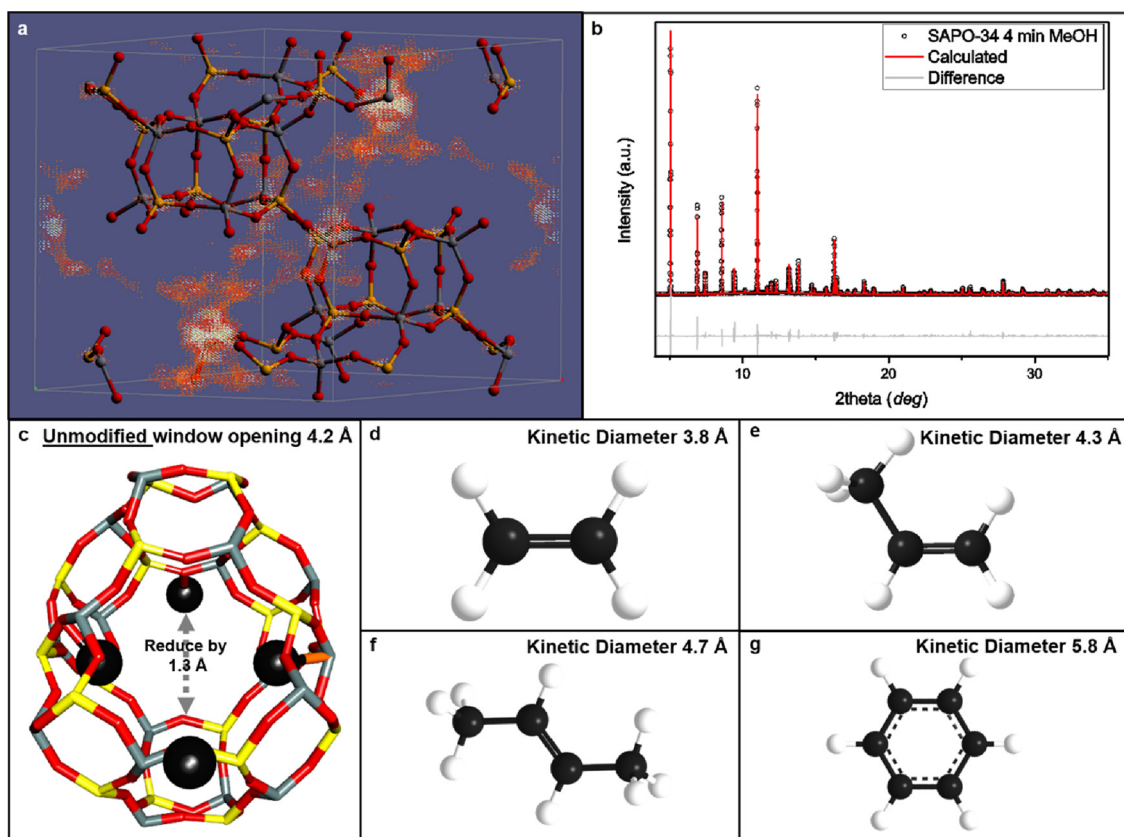


**Fig. 2.** (a) Fourier contrast map generated from the SXR measurement after 4 min-TOS of MeOH injection (calculated by  $F_{obs}-F_{calc}$  in TOPAS v.4.2); the brighter regions/patches suggest higher electron density, (b) the corresponding SXR pattern and Rietveld refinement profile fitted with 12 'C' atoms (zoom-in displayed in Figs. S5–S6 in SM). (c) Rietveld derived crystal structure of framework atoms, the 8-MR pore opening can be reduced by as much as 1.3 Å in one dimension (estimated by the CrystalMaker software). Its aperture is smaller than the kinetic diameters of the molecules studied. Grey = Si/Al, yellow = P, red = O, and black = C. No hydrogens are plotted for clarity. (d) – (g) Displays of ethylene, propylene, trans-2-butene, and benzene, with their corresponding estimated kinetic diameters [34]. Ball-and-stick model: grey = Si/Al, yellow = P, and red = O. (For interpretation of the references to colour in this figure legend, the reader is referred to the web version of this article.).

of CO, HCHO,  $CH_4$ ; only these selected fragments ions were monitored by MS).

As seen in Fig. 1(a), the relative  $C_2^= + C_3^=$  selectivity increases from ca. 83% to 88% at the expense of  $C_4^=$  (from ca. 16% to 11%) agrees with the industrial observation. It is achieved at virtually

completed methanol conversions over the given TOS from 1 to 10 min in this small capillary reactor system (a significant shorter induction period due to shorter residence time compared to the industrial reactor). The corresponding SXR patterns are displayed in Fig. 1(b). The effect of flowing methanol is apparent as seen in the early 20 Bragg

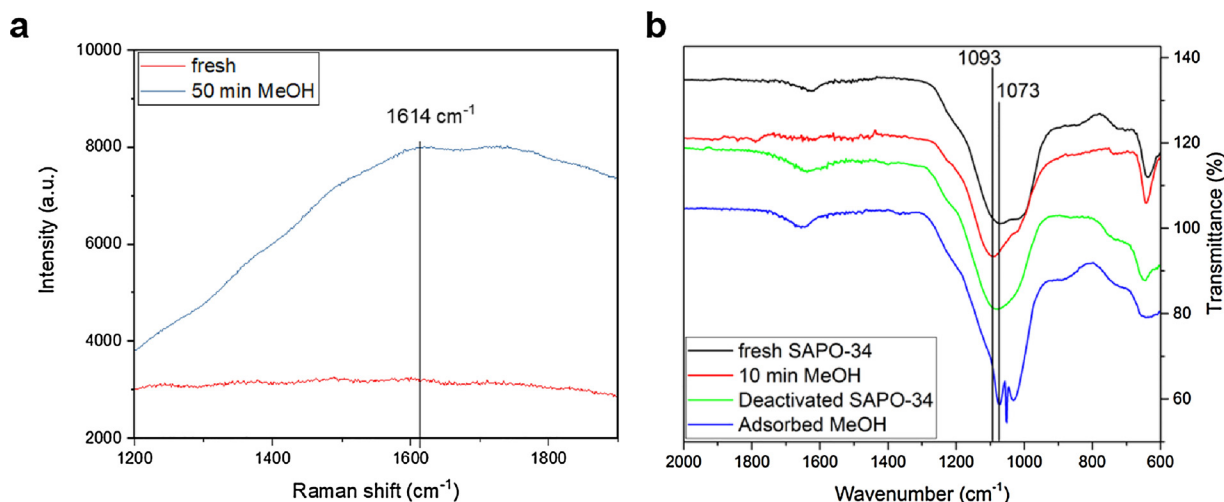


**Fig. 3.** (a) Raman spectra showing fresh and spent SAPO-34 samples. An extra feature at  $1614\text{ cm}^{-1}$  has been observed, which corresponds to monocyclic carbon species [31]. (b) FT-IR spectra of various treated SAPO-34 samples. An extra feature can be observed at  $1100\text{ cm}^{-1}$  for the SAPO-34 sample after 10 min of time-on-stream. This corresponds to a typical C–O stretching mode [15].

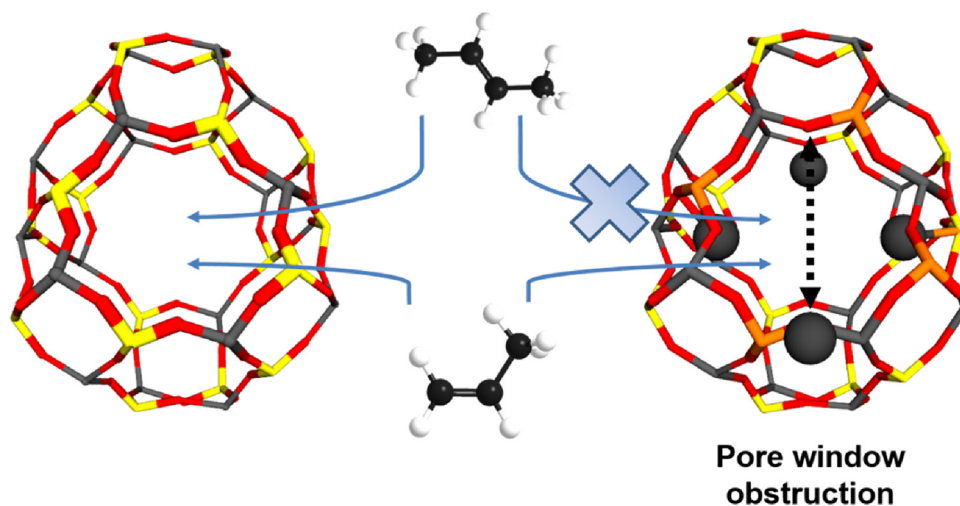


**Fig. 4.** Illustration of the pore window obstruction of SAPO-34. Briefly, due to the formation of the SMS, the 8-MR pore opening of SAPO-34 becomes smaller to further deny larger  $n\text{-C}_4$  species to pass through.

peaks, where a notable fall in the peak intensity can be seen. This can be attributed to the filling of the pores in SAPO-34. Consistent with the work by Wragg et al. [25–27], the lattice slightly expands in volume due to carbon infiltration to the crystal upon longer TOS (see the crystallographic parameters in Table S1 in SM). Despite the differences in the applied pressure and flow characteristics from those collected in Table 1, both sets of experiments indicate that the  $\text{C}_2 = + \text{C}_3 =$  selectivity progressively increases at the expense of higher olefins during the induction period. Although we did not measure the SXRD of the SAPO-34 sample for longer TOS, one can see the fast growth in SMS population in the first 6 min and rapidly levelling at further time. It appears from the Fig. 1a that the SMS population is progressing to a plateau. Also, the product selectivity stabilises reaching steady state after the first 6 min of TOS.

The Fourier contrast map that displays the electron density for the SXRD measurement after 4-min TOS (see Fig. 2(a), generated by TOPAS v.4.2) indeed shows a small amount of ‘carbonaceous’ species in the SAPO-34 cavity at the early stage of induction. However, these carbon levels do not seem to offer much blockage to the cavity nor the pore opening. To check whether carbon atoms are deposition on the framework, the Rietveld refined SAPO-34 crystal is shown in Fig. 2(c) (showing the SAPO-34 framework without the extra-framework ‘C’

atoms). It is interesting to observe an isolated ‘C’ (notice that H atoms cannot be detected or refined by this technique) is found attached to framework O atom at a bond distance of ca.  $1.5\text{ Å}$ . The presence of this isolated ‘C’ can be confirmed by 10 repeated attempts in physically locating it away from the framework, where it returned to this framework position under the energy minimisation process. The Rietveld refinement has reached the global minimum with a closely-fitted profile and a  $R_{\text{wp}}$  value of 10.67% (see Fig. 2(b) and Figs. S2–S3 in SM). Note that the  $B_{\text{eq}}$  values (isotropic displacement factors) of the ‘C’ atoms have been fixed at  $5\text{ Å}^2$  to ensure the consistency and reliability of the site occupancy factors (see references for the refinement work for their acceptable  $R_{\text{wp}}$  of ca. 20% measured at room temperature by van Koningveld et al. [28], Fitch et al. [29] and Mentzen et al. [30], etc.). The formation of the carbonaceous species is also supported by Raman spectroscopy (see Fig. 3(a)). The spent samples show an extra feature at  $1614\text{ cm}^{-1}$ , which corresponds to a few monocyclic carbons in the zeolite cavity [31]. We have also verified the total carbon (derived from the Rietveld refinement) by comparing it against that deduced from the thermogravimetric analysis (TGA) (see Figure S4 in SM).

The presence of the SMS can be attributed to methanol dehydration over the BAS that forms adsorbed SMS ( $\text{CH}_3\text{-O}_z$ , where  $\text{O}_z$  is a framework oxygen atom) from the dissociative mechanism [32]. The



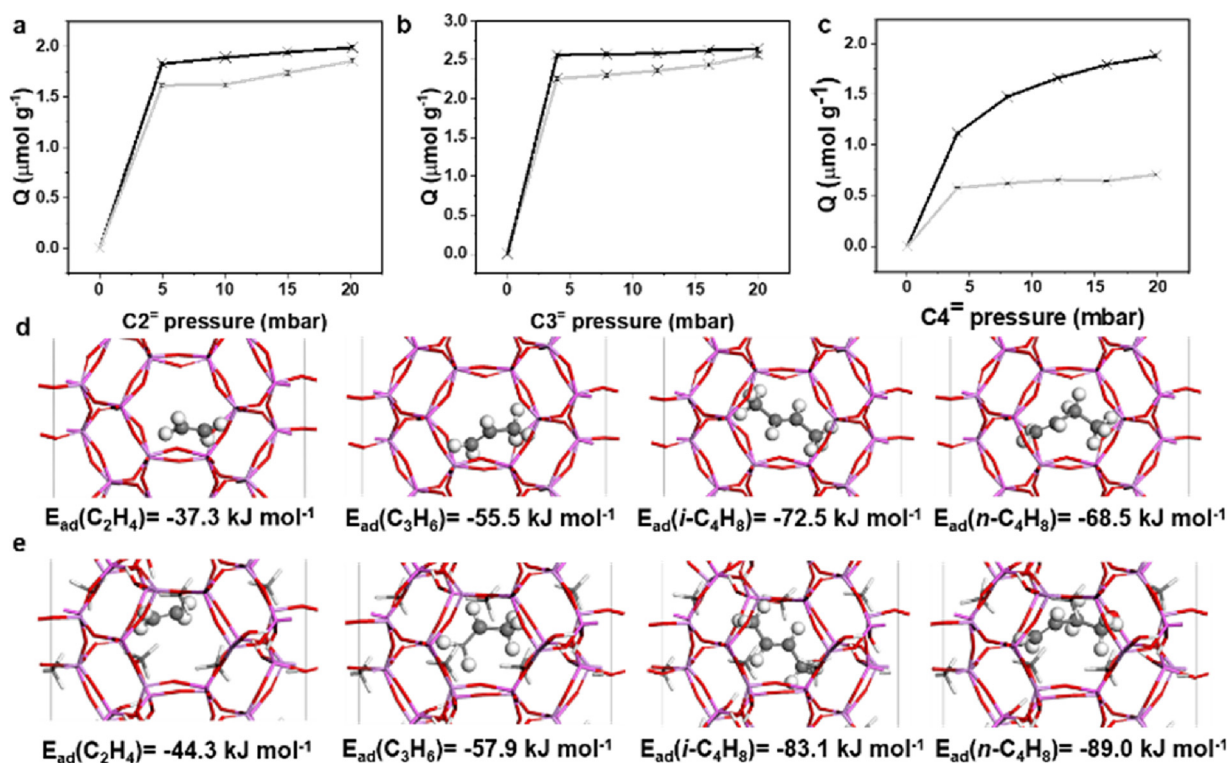


Fig. 5. Adsorption study of fresh (black line) and spent (30-min TOS, grey line) SAPO-34 samples using intelligent gravimetric analysis with (a) ethylene, (b) propylene, and (c) trans-2-butene. Periodic DFT calculated adsorption energies of ethylene, propylene, i-butene and trans-but-2-ene in the (d) fresh and (e) spent SAPO-34 samples.

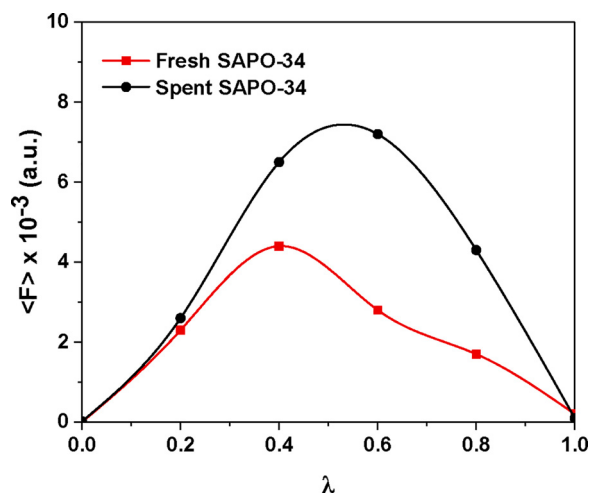


Fig. 6. The averaged mean force ( $\langle F \rangle$ ) as a function of the constraint parameter ( $\lambda$ ) for ethylene in fresh and spent SAPO-34 zeolites.

Table 2

Estimated free energy barriers for diffusion ( $\text{kJ mol}^{-1}$ ) in the fresh and spent SAPO-34 samples of ethylene, propylene, i-butene, and trans-2-butene.

Sample	Ethylene	Propylene	i-butene	Trans-2-butene
Fresh SAPO-34	16.7	18.9	34.6	36.7
Spent SAPO-34	24.8	33.2	66.3	74.3

population of this SMS is also found to increase progressively and then level off along with increasing TOS, which suggests that the SMS forms part of the framework under the dynamic methanol flow during the induction period (see Fig. 1(a), and Table S2 in SM). Also, from the FT-IR spectrum (see Fig. 3(b)), the significant change in peak intensity at

ca.  $1100\text{ cm}^{-1}$  reinforces the existence of the newly formed C–O on the BAS [33].

It is intriguing that the original framework of SAPO-34 can be subtly modified by the newly formed SMS, as seen in Fig. 2(c): the 8-membered ring (MR) pore opening in molecular dimension is therefore obstructed by the SMS. This should exert a great influence on the diffusivities of the gas products (the estimated kinetic diameters from their molecular weights are shown in Fig. 2(d)–(g) [34]). An unmodified SAPO-34 has a pore opening of  $4.2\text{ \AA}$  (and a cage diameter of  $8.0\text{ \AA}$ ), which offers molecular sieving to deny larger molecules like benzene from the HCP intermediate to pass through the window [35] (see Fig. 2(g)). However, the window dimension is larger than  $\text{C}_2^\equiv/\text{C}_3^\equiv$ , but is comparable to  $\text{C}_4^\equiv$ . Due to the obstruction of the pore opening by the SMS, intrinsically larger i-/n-butene molecules are circumvented from passing through. An illustration of this idea is presented in Fig. 4. Thus, the overall rate of product distribution progressively leans towards the more industrially significant  $\text{C}_2^\equiv + \text{C}_3^\equiv$  products, which matches well with the rate of increase in the population of SMS (see Fig. 1(a) and Table S2 in SM) during the induction period.

As a result, the change in the product selectivity is attributed to the mass transport effect through molecular sieving by the modification of the 8-MR pore window in a dynamic manner. Note that methanol decomposition provides a steady source of methyl as the molecular obstacle as well as for HCP formation. We also noted the activity of SAPO-34 began to drop significantly after 14-min of TOS, while the population of the SMS had well reached a plateau. This implies that the deactivation of SAPO-34 is correlated to the accumulation of carbonaceous species at a longer TOS rather than the dynamic SMS concentration which mainly alters the olefinic selectivity, as that observed from the macroscopic catalytic performance.

To further investigate experimentally how a working SAPO-34 catalyst is modified during the MTO process, we performed a series of gas adsorption studies over the fresh and spent (10-min TOS) samples by intelligent gravimetric analysis (see Fig. 5(a)–(c), see experimental

details in SM/Methods). For ethylene and propylene, the gas adsorption capacity ( $Q$ ) is found to be only mildly affected by about 10–15%, depending on the pressure of the applied gas. However, the structural modification effect is more apparent in the case of trans-2-butene, where the spent SAPO-34 sample only adsorbs 31% of that of the fresh SAPO-34 at 20 mbar of trans-2-butene. This shows the remarkable size sieving effect on the larger trans-2-butene species that is physically hindered to diffuse through the modified 8-MR pore windows. The periodic DFT calculations had also been performed to understand the effects of SMS on the adsorption and diffusion behaviours of four selected MTO products (ethylene, propylene, i-butene and trans-2-butene).

As shown in Fig. 5(d)–(e), the adsorptions of both  $C_4^=$  isomers are generally stronger than the  $C_2^=$  and  $C_3^=$  species, aligning with their molecular masses (adsorption of homologue hydrocarbons have experimentally correlated to their boiling points [36]). With an increasing SMS concentration in the spent SAPO-34 zeolite, the interactions of all four products become stronger. It suggests that the higher non-polar affinity of SMS to these olefins (or stronger van der Waal's dispersion). We noted that the extent for the enhancement in the adsorption energies for both  $C_4^=$  isomers over the spent SAPO-34 catalyst with an increasing SMS coverage ( $10\text{--}20\text{ kJ mol}^{-1}$ ) are higher than those of  $C_2^=$  and  $C_3^=$  ( $< 7\text{ kJ mol}^{-1}$ ). This suggests that the migration of the  $C_4^=$  isomers within the cages becomes more difficult, whereas  $C_2^=$  and  $C_3^=$  species are less affected. To further confirm the inhibiting effects on the migration of the olefin products, the free diffusion energy barrier ( $\Delta F$ ) of each olefin species between two neighbouring cages through the 8-MR pore window was calculated (see Fig. 6) and the free diffusion energy barriers for each species were also summarised in Table 2. Compared with the fresh SAPO-34 sample, it was found that the diffusion barriers are nearly doubled in the presence of SMS. The presence of SMS at the 8-MR pore window in the spent SAPO-34 dramatically inhibited the diffusion of the MTO products, especially for larger size molecules like the  $C_4^=$  isomers. Thus, it is expected that the  $C_4^=$  products are significantly reduced by the SMS, with the SMS acting as a physical barrier and a modifier to enhance adsorption/storage in the spent SAPO-34. This leads to a lower  $C_4^=$  selectivity after the induction period. Meanwhile, the diffusion of lower olefin species is only marginally affected as that observed experimentally.

## 5. Conclusion

In short summary, it is demonstrated from using synchrotron X-ray powder diffraction and Rietveld refinement and that the molecular sieving properties of SAPO-34 can be dynamically modified in favour of lower olefins production due to the meta-stable SMS formation on the BAS near the pore opening during the early induction period of the MTO process. Further modifications of pore structure and adsorption properties of the zeolite by the building-up carbonaceous deposition are also anticipated at longer TOS. We believe that this work will offer additional and alternative insights to the 'dual cycle' mechanistic study of the catalytic methanol-to-olefins process. There is certainly a greater degree of error when X-ray based techniques are solely used to study lighter elements. It is noteworthy that neutron-based (or in combination with synchrotron X-ray) techniques have been previously employed since the late 1990s to probe the atomic information of the molecular species like benzene in zeolites, due to their low X-ray scattering parameters [2]. However, the complex neutron instrumentation leads to various technical difficulties in carrying out in situ catalytic studies [3]. Specially designed in situ reactor cells are required to be carefully

designed for such in situ neutron experiments. On the other hand, owing to the optimisation of the modern SXRD instrumental set-up, SXRD experiments that are more closely related to catalysis chemistry have recently been carried out and generally accepted by the community, notably by the extensive works from Wragg and co-workers and our group [3–16].

## Appendix A. Supplementary data

Supplementary material related to this article can be found, in the online version, at doi:<https://doi.org/10.1016/j.apcatb.2018.05.090>.

## References

- [1] G.A. Olah, A. Goepfert, G.K.S. Prakash, *Beyond Oil Gas Methanol Econ*, second ed., (2009), pp. 1–334.
- [2] Y. Ono, T. Mori, J. Chem. Soc. Faraday Trans. 1 (77) (1981) 2209–2221.
- [3] Y. Ono, T. Baba, Phys. Chem. Chem. Phys. 17 (2015) 15637–15654.
- [4] I.M. Dahl, S. Kolboe, Catal. Lett. 20 (1993) 329–336.
- [5] B. Arstad, S. Kolboe, J. Am. Chem. Soc. 123 (2001) 8137–8138.
- [6] M. Bjoergen, S. Svelle, F. Joensen, J. Nerlov, S. Kolboe, F. Bonino, L. Palumbo, S. Bordiga, U. Olsbye, J. Catal. 249 (2007) 195–207.
- [7] M. Bjoergen, U. Olsbye, S. Kolboe, J. Catal. 215 (2003) 30–44.
- [8] M. Bjoergen, S. Akyalcin, U. Olsbye, S. Benard, S. Kolboe, S. Svelle, M. Bjoergen, S. Akyalcin, U. Olsbye, S. Benard, S. Kolboe, S. Svelle, J. Catal. 275 (2010) 170–180.
- [9] S. Svelle, F. Joensen, J. Nerlov, U. Olsbye, K.-P. Lillerud, S. Kolboe, M. Bjoergen, J. Am. Chem. Soc. 128 (2006) 14770–14771.
- [10] M. Luo, H. Zang, B. Hu, B. Wang, G. Mao, RSC Adv. 6 (2016) 17651–17658.
- [11] D. Lesthaeghe, J. VanderMynsbrugge, M. Vandichel, M. Waroquier, V. VanSpeybroeck, ChemCatChem 3 (2011) 208–212.
- [12] U. Olsbye, S. Svelle, M. Bjoergen, P. Beato, T.V.W. Janssens, F. Joensen, S. Bordiga, K.P. Lillerud, M. Bjoergen, P. Beato, T.V.W. Janssens, F. Joensen, S. Bordiga, K.P. Lillerud, Angew. Chem. Int. Ed. 51 (2012) 5810–5831.
- [13] M. Stöcker, Microporous Mesoporous Mater. 29 (1999) 3–48.
- [14] D.H. Olson, N. Khosrovi, A.W. Peters, B.H. Toby, J. Phys. Chem. B 104 (2000) 4844–4848.
- [15] T. Suzuki, T. Okuhara, Microporous Mesoporous Mater. 43 (2001) 83–89.
- [16] B.P.C.C. Hereijgers, F. Bleken, M.H. Nilsen, S. Svelle, K.-P.P. Lillerud, M. Bjoergen, B.M. Weckhuysen, U. Olsbye, J. Catal. 264 (2009) 77–87.
- [17] J. Jae, G.A. Tompsett, A.J. Foster, K.D. Hammond, S.M. Auerbach, R.F. Lobo, G.W. Huber, J. Catal. 279 (2011) 257–268.
- [18] C. Wang, Y. Chu, A. Zheng, J. Xu, Q. Wang, P. Gao, G. Qi, Y. Gong, F. Deng, Chem. Eur. J. 20 (2014) 12432–12443.
- [19] B.T.W. Lo, L. Ye, J. Qu, J. Sun, J. Zheng, D. Kong, C.A. Murray, C.C. Tang, S.C.E. Tsang, Angew. Chem. Int. Ed. 55 (2016) 5981–5984.
- [20] L. Ye, B.T.W. Lo, J. Qu, I. Wilkinson, T. Hughes, C.A. Murray, C.C. Tang, S.C.E. Tsang, Chem. Commun. 52 (2016) 3422–3425.
- [21] I.F. Teixeira, B.T.W. Lo, P. Kostetsky, M. Stamatakis, L. Ye, C.C. Tang, G. Mpourmpakis, S.C.E. Tsang, Angew. Chem. Int. Ed. 55 (2016) 13061–13066.
- [22] E.S.C. Tsang, L. Ye, B. Lo, Q. Song, J. Zheng, D. Kong, C. Tang, Angew. Chem. Int. Ed. 56 (2017) 10711–10716.
- [23] L. Ye, I.F. Teixeira, B.T.W. Lo, P. Zhao, S.C. Edman Tsang, E. Tsang, Chem. Commun. 53 (2017) 9725–9728.
- [24] S.P. Thompson, J.E. Parker, J. Marchal, J. Potter, A. Birt, F. Yuan, R.D. Fearn, A.R. Lennie, S.R. Street, C.C. Tang, J. Synchrotron Radiat. 18 (2011) 637–648.
- [25] D.S. Wragg, M.G. O'Brien, F.L. Bleken, M. Di Michiel, U. Olsbye, H. Fjellvåg, Angew. Chem. Int. Ed. 51 (2012) 7956–7959.
- [26] D.S. Wragg, R.E. Johnsen, M. Balasundaram, P. Norby, H. Fjellvåg, A. Grønvd, T. Fuglerud, J. Hafizovic, Ø.B. Vistad, D. Akporiaye, J. Catal. 268 (2009) 290–296.
- [27] D.S. Wragg, D. Akporiaye, H. Fjellvåg, J. Catal. 279 (2011) 397–402.
- [28] H. Van Koningsveld, Acta Crystallogr. Sect. B Struct. Sci. 46 (1990) 731–735.
- [29] R. Goyal, A.N. Fitch, H. Jobic, J. Phys. Chem. B 104 (2000) 2878–2884.
- [30] B.F. Mentzen, Mater. Res. Bull. 22 (1987) 489–496.
- [31] D.S. Wragg, A. Grønvd, A. Voronov, P. Norby, H. Fjellvåg, Microporous Mesoporous Mater. 173 (2013) 166–174.
- [32] A. Ghorbanpour, J.D. Rimer, L.C. Grabow, ACS Catal. 6 (2016) 2287–2298.
- [33] J.S. Huberty, R.J. Madix, Surf. Sci. 360 (1996) 144–156.
- [34] J. Koresch, A. Soffer, J. Chem. Soc. Faraday Trans. 1 Phys. Chem. Condens. Phases 76 (1980) 2472–2485.
- [35] C.D. Baertsch, H.H. Funke, J.L. Falconer, R.D. Noble, J. Phys. Chem. 100 (1996) 7676–7679.
- [36] K.A. Campbell, M.J. Janik, R.J. Davis, M. Neurock, Langmuir 21 (2005) 4738–4745.